



Published in final edited form as:

Anal Chem. 2023 September 05; 95(35): 13172–13184. doi:10.1021/acs.analchem.3c02073.

Monitoring Metabolic Changes in Response to Chemotherapies in Cancer with Raman Spectroscopy and Metabolomics

Gabriel Cutshaw^{a,b,†}, Nora Hassan^{a,b,†}, Saji Uthaman^{a,b}, Xiaona Wen^b, Bhuminder Singh^c, Anwesh Sarkar^{d,*}, Rizia Bardhan^{a,b,*}

^aDepartment of Chemical and Biological Engineering, Iowa State University, Ames, IA 50011, USA

^bNanovaccine Institute, Iowa State University, Ames, IA 50012, USA

^cDepartment of Medicine, Vanderbilt University Medical Center, Nashville, TN 37232, USA

^dDepartment of Electrical Engineering, Iowa State University, Ames, IA 50012, USA

Abstract

Resistance to clinical therapies remains a major barrier in cancer management. There is a critical need for rapid and highly sensitive diagnostic tools that enable early prediction of treatment response to allow accurate clinical decisions. Here we employ Raman spectroscopy to monitor changes in key metabolites as early predictors of response in *KRAS* mutant colorectal cancer (CRC) cells, HCT116, treated with chemotherapies. We show at the single cell level that HCT116 is resistant to cetuximab, the first-line treatment in CRC, but this resistance can be overcome with pre-sensitization of cells with oxaliplatin. In combination treatment of cetuximab + oxaliplatin, we observed that sequential delivery of oxaliplatin followed by cetuximab rather than simultaneous administration of drugs is critical for effective therapy. We also demonstrated that metabolic changes are well aligned to cellular mechanical changes where Young's modulus decreased after effective treatment indicating both changes in mechanical properties and metabolism in cells are likely responsible for cancer proliferation. Raman findings were verified with mass spectrometry (MS) metabolomics, and both platforms showed changes in lipids, nucleic acids, and amino acids as predictors of resistance/response. Finally, we identified key metabolic pathways enriched when

*Corresponding authors: rbardhan@iastate.edu; anweshas@iastate.edu.

†Equal contributing first authors

Author contributions

RB conceived the project idea, directed the study design, and edited the manuscript. GC performed most of the data analysis, data interpretation, and wrote the manuscript. NH conducted all Raman spectroscopy, cell culture experiments and wrote part of the manuscript. SU trained NH and GC in cell culture techniques and other biological material handling, and edited the manuscript. XW trained GC and NH in Raman sample preparation, Raman analysis, Raman measurements, and edited the manuscript. BS provided the cancer cell lines, insight on treatment combinations and expected metabolic changes, and edited the manuscript. AS performed all the AFM measurements and wrote that part of the manuscript.

Conflicts of interest

The authors declare no conflict of interest.

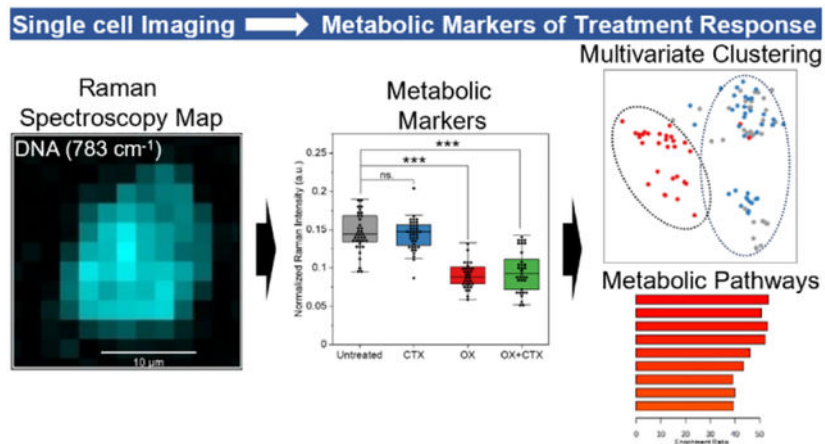
Supporting Information Available:

This material is available free of charge via the Internet at <http://pubs.acs.org>.

Materials and methods, high resolution Raman image of single cells, PC loadings, comparison of Raman peak values between untreated and CTX treated HCT116 cells, cell viability for simultaneous oxaliplatin & CTX combinatorial therapy, comparison of Raman peak values between CTX-treated and combinatorial-treated HCT116 cells, metabolite contributions to pathway enrichment, LC-MS pathway enrichment comparisons for untreated and CTX-treated cells, and untreated and combinatorial-treated cells.

cells are resistant to cetuximab but downregulated with effective treatment. Our study highlights that drug-induced metabolic changes both at the single cell level (Raman) and ensemble level (MS) has the potential to identify mechanisms of response to clinical cancer therapies.

Graphical Abstract



Keywords

Raman spectroscopy; metabolomics; cancer; machine learning; metabolism; treatment response; mechanical properties

1. Introduction:

Colorectal cancer (CRC) is the third most common cancer diagnosed globally,¹ and represents 9% of all new cancer cases in the U.S.² Whereas patients with localized disease have a high survival rate, metastatic CRC is lethal with a 5-year survival of ~13%.³ Genomic characterization combined with immunohistochemistry analysis of tumors remains the standard practice to guide initial treatment choices.⁴ However, patients diagnosed with CRC have limited therapeutic options. Many patients are resistant to anti-EGFR (epidermal growth factor receptor) therapies, the first-line treatment for CRC.⁵ For unresectable tumors, chemotherapies and radiation are often applied as neoadjuvant (before surgery) or adjuvant (after surgery) treatment to achieve tumor reduction. Among the current chemotherapy regimen for CRC patients, a combination of fluoropyrimidine (5-FU) and oxaliplatin (OX), coined as FOLFOX, have been highly effective.⁶ However, inter- and intratumor heterogeneities contribute to *de novo* and acquired resistance to these therapies resulting in metastatic disease.⁷⁻⁹ There is an urgent clinical need for highly sensitive diagnostic tools that can accurately predict treatment response and guide clinicians on the most effective therapies at the earliest time points. Further, early identification of patients resistant to therapies will also minimize unjustified toxicities and the high costs of unsuccessful treatment.

It is well known that cancer cells dynamically alter their metabolic processes to maintain viability.¹⁰ Early observations by Otto Warburg suggested that cancer cells consume copious

amounts of glucose to generate lactate via aerobic glycolysis, now coined as Warburg effect. Recent findings show cancer cells also leverage the tricarboxylic acid (TCA) cycle to provide necessary metabolites for growth and nicotinamide adenine dinucleotide phosphate (NADPH) production.¹⁰ Anabolic pathways also play a critical role in cancer metabolism where simple nutrients such as amino acids are converted into biosynthetic intermediates that ultimately control proteins, lipids, and nucleotides synthesis.¹¹ Ultimately, these metabolites converse onto oncogenic pathways such as *KRAS* and *BRAF* signaling protein gene mutations that are prevalent in CRC, as well as promote immunosuppressive immune cells and inhibit the function of cytotoxic CD8⁺ T cells.¹² Since metabolic reprogramming in cancer cells occurs at a much earlier time point before macroscopic changes in tumor burden is observable,¹³ it is hypothesized that assessment of drug-induced metabolic changes could enable early prediction of therapeutic response or resistance in a clinical setting, and determine drivers of tumorigenesis.

In this work, we demonstrate the utility of Raman spectroscopy for metabolic profiling in *KRAS* mutant human CRC cells to understand pathways associated with resistance to anti-EGFR (cetuximab) therapies and response to OX treatment. Raman spectroscopy (RS) is a noninvasive optical approach that is emerging as a contender for rapid and highly sensitive metabolic profiling relative to traditional approaches such as magnetic resonance spectroscopy.^{14–16} In RS, when a sample interacts with incident light, inelastic scattering of these incident photons causes transitions between vibrational states. A monochromatic laser is used as the source of incident photons, and by measuring the change in the energy/frequency of the laser, the sample's biochemical fingerprint is revealed.^{17, 18} RS is an inexpensive approach that enables spatiotemporal distribution of drug-induced metabolic changes at single cell resolution *in vitro*. Due to its high sensitivity, RS has enabled both live cell imaging and real-time *in vivo* spectral measurements.^{19–24} RS is also a label-free, stain-free, and extraction-free method allowing direct measurement of samples without cost- and time-intensive preparation steps, and since RS is nondestructive, samples can be archived for future analysis. Bardhan and co-workers, and others have leveraged these merits of RS for measurements in cells, tissues, and biofluids, and RS has also been used with nanoparticles as surrogates for assessing biomarker distribution and therapeutic response.^{25–31}

Here we show RS captures drug-induced metabolic changes in human CRC cells, HCT116, in response to clinical drugs cetuximab (CTX), OX, and a combination of OX + CTX. CCK-8 ensemble viability assays were used to screen for the IC₅₀ of monotherapy and combination treatment. Raman spectral measurements were then differentiated between responsive and nonresponsive treatment groups with principal component analysis (PCA) of the collected data. Raman spectral data was assessed with principal component analysis (PCA) to distinguish cells that are responsive to treatment from those resistant. RS showed HCT116 cells are resistant to CTX but responsive to OX, and that in combination treatment, sequential delivery rather than simultaneous administration of drugs is critical for effective therapeutic response. RS identified the metabolic signal changes associated with effective OX and combination treatment, allowing us to assess the therapeutic efficacy at the single cell level. We also showed metabolic changes correspond well to mechanical changes in cells measured with atomic force microscopy (AFM) where cellular elasticity or stiffness (Young's modulus) decreased but cellular deformation increased for cells responsive to OX

treatment. Our findings show that mechanosignaling and metabolism are linked in cancer cells where treatment-resistant cells maintain their structural integrity and regulate their metabolic needs to continue proliferation.³² Further, we verified metabolites identified with RS with mass spectrometry (MS) metabolomics, and both platforms collectively show that fatty acids, amino acids, and nucleic acids among others are specifically altered in the combination treatment group. RS and MS are complementary approaches where ensemble cellular measurement (millions of cells) of MS is synergistic to metabolic changes measured in single cells with RS. We also identified key metabolic pathways using Kyoto Encyclopedia of Genes and Genomes (KEGG) pathway analysis that are enriched in cells responsive to OX, and OX + CTX combination treatment, and how those pathways are reprogrammed when cells are resistant to CTX. Our study highlights that metabolic and mechanical assessment at the single cell level captures heterogeneous drug response that are key to identifying resistance mechanisms to standard of care therapies in CRC.

2. Results and Discussion

We evaluated treatment response or resistance to clinical drugs CTX and OX with CCK-8 cell viability assay to determine the IC₅₀ (50% of viable cells) of drugs in HCT116 cells. Viability was assessed after subtracting blanks relative to cells grown in untreated media. The trendline was fit and the IC₅₀ was calculated by a GraphPad Prism nonlinear fit using the “log(inhibitor) vs. normalized response” model. Complete experimental methods for the cellular viability assays are provided in the supporting information. Cells treated with OX for 48 h had an IC₅₀ of 2.7 μ M (95% CI of 2.4 to 3.0) whereas HCT116 was resistant to CTX even up to a high concentration of 400 nM (Fig. 1a). Since the cells were responsive to OX monotherapy, cells were then plated on poly-L-lysine (PLL) treated CaF₂ disks to collect RS maps on single cells. Samples were excited with a 785 nm laser with a power of ~50 mW focused on the sample using a 100X objective. We measured >30 cells per sample where each cell was measured at a grid resolution of 2 μ m, resulting in 90 – 200 points per map. Each spectrum was collected with 15 s exposure time and 2 accumulations (30 s total per point) resulting in mapping times of 45 to 100 min. An example of the optical and RS image of a single cell is shown in the supporting information (Fig. S1). The spectral map was averaged over the whole cell to generate a single representative spectrum per cell. The data was normalized using the standard normal variate method,³³ and then subjected to a ratiometric analysis with the 1448 cm⁻¹ lipid/protein peak to allow for quantitative comparisons between peak values.³⁴ The 1448 cm⁻¹ peak was chosen for the ratiometric normalization since it varies minimally between individual cells and the treatment groups. Detailed signal processing methodology can be found in the experimental methods section in the supporting information. The average spectrum of OX-treated HCT116 cells show significant differences in peak intensities relative to untreated control while the spectrum for the CTX-treated cells shows a minimal difference from the control (Fig. 1b, c), confirming HCT116 is resistant to CTX. PCA was used as a dimensionality reduction and unsupervised clustering and classification tool. PCA shows a clear clustering of OX-treated cells relative to untreated control and CTX-treated cells, which cluster together (Fig. 1d). Here, the principal components PC1, PC2 and PC3 are responsible for 65.56%, 15.61% and 4.18% of the variability of the dataset, respectively. The PC loadings for PC1 and PC2 are provided in

the SI (Fig. S2a), which support the Raman difference spectra and is a good representation of the difference in the spectral profiles of the cell populations. From the PCA clustering, only 2 cells from the OX treated cells show misclassification i.e. they cluster with the untreated control/CTX treated cells, which is not surprising as cancer cells often show heterogeneous response/resistance to chemotherapies.

We then identified 32 statistically significant peaks in RS using a student's t-test with the false discovery rate correction and corresponding metabolites that differentiated OX-treated cells from untreated control (Fig. 1e); 28 of these metabolites decreased in the treatment group and 4 metabolites increased. To associate RS spectral data with specific metabolites and metabolite classes, we referred to the cited literature in Table 1 that reports well-established RS peaks for key metabolites.^{35–39} Tentative peak assignments were narrowed down based on literature on metabolites that are impacted in human colorectal cancer, and cellular metabolites that change in response to treatment; these literature evidence supported the assigned Raman peaks to the metabolites we have listed.^{11, 40–49} As each RS peak arise from vibrational modes within a functional group, a specific peak is not exclusive to a metabolite. Therefore, our tentative peak assignments represent the most plausible major metabolites that contribute to these peaks.

We observed that peaks corresponding to DNA bases including 648 cm^{-1} , 783 cm^{-1} , and 1575 cm^{-1} had significant decreases, aligning well with the cytotoxic action of OX and its ability to arrest the cell cycle and prevent further DNA replication.^{50–52} The evidence of damage from DNA-platinum adducts is also observed as a decrease in peaks corresponding to RNA chain structure (811 cm^{-1}) and amino acids including histidine (1316 cm^{-1}), phenylalanine (622 cm^{-1} , 1003 cm^{-1} , 1031 cm^{-1} and 1605 cm^{-1}), proline (643 cm^{-1}), threonine (1340 cm^{-1}), tyrosine (828 cm^{-1}) and tryptophan (757 cm^{-1} and 1555 cm^{-1}). Platinum-DNA adducts hamper RNA transcription in addition to DNA replication by inhibiting the binding capacity of RNA polymerase, leading to a reduction in protein and amino acid synthesis.^{51, 53} OX treatment of cells also leads to dysregulation of lipid metabolism; we observed a decrease in peaks associated with membrane phospholipids (722 cm^{-1}) and saturated fatty acids (958 cm^{-1} , 1088 cm^{-1} and 1174 cm^{-1}). We also observed a decrease in the glucose peak (1126 cm^{-1}); cancer cells meet their energy demand primarily via aerobic glycolysis and therefore treatment with OX is expected to suppress the glucose to lactate production, which manifests as a decrease in the glucose peak in RS.^{49, 54} We also observed several metabolites increased in the OX treated group including RS peaks associated with the cholesterol ring structure (701 cm^{-1}), triglycerides (1300 cm^{-1}), and the vibration of C=C in unsaturated lipids (1658 cm^{-1}) that include membrane phospholipids such as phosphatidylcholine (PC) and phosphatidylethanolamine (PE). These findings align well with previous studies of apoptotic cancer cells with NMR spectroscopy that showed similar lipid dysregulation including decrease in PC,^{43, 55, 56} accumulation of triglycerides,⁵⁵ and an increase in lipid unsaturation.⁵⁶ Triglycerides and cholesterol are associated with cell signaling events and with apoptosis, and can trigger caspase-1 activation.⁴⁶ The cells treated with CTX showed minimal metabolic changes relative to the untreated control and all 30 major peaks had no statistically significant differences (Figure S3). This is expected as HCT116 is KRAS-mutant where the constitutive activation of KRAS limits the ability of anti-EGFR antibodies to block the signaling pathways

downstream of the EGFR tyrosine kinase.⁵⁷ We also performed preliminary supervised learning analysis with PLS-DA using the spectral peak data (Figure S2b). Unlike PCA, which performs dimensionality reduction to identify directions of intra-sample variability, PLS-DA performs dimensionality reduction to maximize variance between classes, thereby serving as a discriminative tool. While the limited sample size of the study limits the supervised methods, PLS-DA can be used to identify metabolic peaks that best discriminate between classes. Variable influence on projection (VIP) scores for the comparison of untreated and oxaliplatin treated cells highlight amino acids such as phenylalanine (1003 cm^{-1}) histidine (1316 cm^{-1}) and threonine (1340 cm^{-1}), DNA (783 cm^{-1} , 1097 cm^{-1} & 1575 cm^{-1}) and Amide III peptide bonds (1250 cm^{-1}) as the most effectively discriminating peaks (Fig. S2c).

Next, we assessed the ability of RS metabolic profiling in distinguishing cells responsive to the combination treatment of OX + CTX to reverse the resistance of HCT116 to CTX. In this combination, simultaneous treatment with both drugs had minimal impact on cell viability relative to OX monotherapy (Fig. S4a). Therefore, we conceded that sequential delivery of the drugs would be therapeutically more effective where sensitization of the cells with OX first renders them susceptible and more responsive to CTX treatment. Our hypothesis was supported by literature findings that confirmed that pre-treatment of EGFR-resistant cells with OX makes them responsive to anti-EGFR antibody treatments.⁵⁸ We treated HCT116 cells with 0 to 200 μM OX for 24 h followed by treatment with 25 nM CTX for an additional 48 h. The control group was treated with OX for 24 h followed by media only for the next 48 h. Cell viability assay of combination treatment (Fig. 2a) showed an IC₅₀ of 2.1 μM OX (95% CI of 1.7 to 2.5), which is less than the IC₅₀ of OX treatment alone (2.7 μM) for 48 h (see Fig. 1a). The combination treatment can also be compared to the control of replacing the OX-treated media with untreated media after 24 h, which showed an IC₅₀ of 4.1 μM OX (95% CI of 3.3 to 5.1) (Fig. 2a). Raman spectra of the combination treatment compared to CTX monotherapy (see Fig. 1b) and corresponding difference spectrum of the two (Fig. 2c) revealed significant metabolic changes resulting from the combination therapy. These differences were also captured in the PCA clustering (Fig. 2d), which shows the distinction between the two groups, and the majority of the variation was observed in PC1 (62.44%) and PC2 (12.24%). In the PCA, each dot represents Raman data of an individual cell. The PC loadings for PC1 and PC2 are provided in the SI (Fig. S5a.) Of the 32 cells in the combination treatment, 6 (18.8%) clustered with the CTX group showing heterogeneity in treatment response. As with the untreated and OX-treated cells, we applied PLS-DA in a preliminary fashion (Figure S5b). VIP scores for the metabolites that separated treated and OX-cells were similar to the VIP scores for metabolites that separated CTX-treated and combination-treated cells. The relative importance of these metabolites showed slight shifts, with Amide III protein bonds (1250 cm^{-1}) and RNA (811 cm^{-1}) rising in importance relative to amino acids such as histidine (1316 cm^{-1}) and threonine (1340 cm^{-1}) (Figure S5c). Comparisons for all metabolic peaks between the CTX-treated and combination treatment cells is shown in Figure S6 We also observed that sequential addition of CTX followed by OX was not effective (Fig. S4b). Our results suggest that to reverse CTX resistance in CRC, first the metabolic and signaling pathways that are reprogrammed in resistant cells should be regulated with chemotherapies.

As CTX is currently only used in RAS wild-type CRC patients, this approach would be highly beneficial for patients with *de novo* and acquired resistance to EGFR blockade therapies.⁵⁹

Metabolic rewiring in cancer cells is not an isolated event as changes in metabolites regulate signaling pathways and control how cells respond to various mechanical and structural cues in their microenvironment.^{10, 60} Indeed mechanosensitive metabolism is rapidly emerging as a process that cancer cells leverage to either “grow or go” choosing to either proliferate at the primary site, or migrate and metastasize at a new site.^{32, 61} During this process, cells regulate their metabolism to meet the energy demand required to proliferate or migrate. For example stiffness of the extracellular matrix (ECM) of tumors increases during growth, and during this process the glucose requirement of cancer cells increases.⁶² Therefore, we conceded that single-cell measurements of mechanical properties of HCT116 cells when correlated to the metabolic activity will provide insight on cancer cell stiffness and how those alter with treatment.

We investigated these properties with quantitative nanomechanical mapping of live HCT116 cancer cells first without any drug (control) using PeakForce QNM mode of atomic force microscopy (AFM).^{63, 64} Peak force QNM mode is an advanced and amplified version of peak force tapping mode of AFM. A force sensor of higher bandwidth compared to the frequency of the periodic interactions is needed for this purpose. In this mode, the modulation frequency is selected to be of much lower value than the resonant frequency (comparable to the force measurement bandwidth) of the cantilever. Complete details are provided in the experimental methods section in the SI. Our approach produces height and peak force error images as well as generates force-distance curve at each pixel of scanning. This mode of AFM is highly useful in generating high-resolution maps of Derjaguin-Muller-Toporov (DMT) modulus, deformation, dissipation, and adhesion.⁶⁵ In order to prevent damage to both live cells and AFM probe, a pre-calibrated specialized Peak Force QNM live-cell probe (PFQNM-LC-A-CAL) with lower stiffness was used for probing HCT116 cells as shown in the phase contrast image of Fig. 3a. The force–distance curves performed at each pixel demonstrating the change of the force acting on the probe vs. tip–sample separating distance were fit with the Hertz model (spherical indenter)⁶⁶ or Sneddon model (conical indenter)⁶⁷ depending on the indentation values to calculate Young’s modulus of HCT116 cells. The Hertz model parameters are given by:

$$F = \frac{4}{3} \cdot \frac{E}{(1 - \nu^2)} \sqrt{R\delta^3/2}$$

where E stands for Young’s modulus, F is the indentation force, δ is the indentation, ν stands for the Poisson ratio (in the range of 0.2–0.5), and R stands for the radius of the indenter.

The Sneddon’s model parameters are given by:

$$F = \frac{2}{\pi} \cdot \frac{E_s}{(1 - \nu_s^2)} \tan \alpha \cdot \delta^2$$

where ν is Poisson's ratio (in the range of 0.2–0.5), E stands for Young's modulus, α is the indenter's half angle, and δ is the indentation, F is the indentation force. If the indentation depth was smaller than the cantilever tip radius (65 nm), the Hertz's model was applied, and if the indentation depth was larger than the tip radius, Sneddon's model was applied. The trend of experimentally measured values does not vary depending on the type of the model used but the values might vary individually. Here, the height, peak force error, DMT modulus, and deformation maps of HCT116 cells without any drug, with OX treatment, and with CTX treatment are shown in Figures 3b–f. The peak force error image represents an approximate measure of regulation error of AFM feedback loop showing an enhanced contrast throughout live cells, and the height sensor image is a rough estimate of the height of the cell. We observed that the Young's modulus or stiffness of cells reduced and cellular deformation increased (Fig. 3e, f) when treated with the responsive drug (OX) compared to untreated control and nonresponsive drug (CTX). The actin cytoskeleton network inside cells is the main force-generating platform; this network allows cells to resist externally generated force by ECM or neighboring cells. The decrease in stiffness and increase in deformation indicates that treatment with OX disrupted the actin polymerization or further actin nucleation that renders cells 'softer' and less likely to proliferate. Since HCT116 cells were resistant to CTX, the cytoskeleton stability of cells treated with CTX was not impacted, and cells maintained their stiffness comparable to the untreated control. Given the crosstalk between cancer cell mechanics and specific metabolites, including glucose and cholesterol (among others), we then examined the changes in these metabolites as a function of treatment with OX and CTX and observed similar trends reflected in Young's modulus (Fig. 3g, h). Cholesterol depletion in cells leads to increased membrane stiffness⁶⁸ can be seen while comparing the relatively cholesterol-enriched OX treated cells and the unenriched nonresponder cells. Further, we also correlated protein peaks in RS to correlate to the cytoskeleton remodeling with OX treatment. The change in protein synthesis is observed in the RS peak analysis of the C-C/C-N stretching protein backbone (1157 cm^{-1} , Fig. 3i) and in the Amide III band (1250 cm^{-1} , Fig. 3j).^{35, 36}

We then validated metabolites identified with RS with liquid-chromatography mass spectrometry (LC-MS) metabolomics of the various sample groups, including untreated control, CTX treated, OX treated, and OX + CTX combination treated cells. The sample processing also included a blank control to subtract background peaks. The complete methodology for sample preparation and LC-MS analysis is provided in the supporting information. A heat map of LC-MS metabolites (Fig. 4) grouped according to metabolite classes showed significant differences between untreated control and CTX (nonresponsive drug) treated cells, and those treated with OX (responsive drug) and combination treatment. For example, we observed a significant decrease in the abundance of membrane phospholipids post-treatment with OX and OX+ CTL combination suggesting a loss of cell membrane integrity due to the initiation of cell death. Since the action of OX occurs primarily through DNA damage, we expected to see differences in nucleic acid-based

metabolites post treatment with OX and combination therapy. Among nucleotides and nucleosides, Inosine triphosphate (ITP), an intermediate in the purine metabolism pathway in ATP and GTP synthesis, showed a marked increase in OX treated group. This finding aligns with previous studies that suggested that p53 activation due to DNA damage serves to regulate Inosine-5'-monophosphate dehydrogenase, thus limiting guanine synthesis.⁶⁹ As RAS signal transduction requires guanine-triphosphate binding, ITP increase suggests incomplete purine metabolism implicating a possible mechanism of anti-EGFR signaling re-sensitization for the resistant HCT116 cells. On the contrary, other nucleotides such as Adenosine monophosphate, a component in RNA synthesis, and Adenosine diphosphate, both crucial for cancer cell growth show a significant decrease in the responsive treatment groups. These results also suggest the inhibition of DNA replication and purine metabolism due to the OX-derived DNA-platinum adducts and p53 activation.^{50, 53} Other metabolic changes observed in RS measurements, such as the reduction in membrane phospholipids and accumulation in triglycerides and cholesterol derivatives, are also evident in the LC-MS results validating our metabolic trends. The distinct changes in diacylglycerol enrichment in the nonresponder group compared to triglyceride enrichment in the responder group may give further insight into the metabolic impact of treatment. Diacylglycerols can be converted into membrane and signaling lipids or converted into triglycerides for energy storage in lipid droplets.⁴¹ Thus the down regulation of proliferative signaling could reprogram the cell's lipid usage and lead to lipid storage. Lipid droplets have been shown to accumulate under stress conditions in CRC and can contribute to chemoresistance.^{45, 70} We also aimed to quantitatively compare the metabolites identified with RS (Fig. 5a) with those obtained with LC-MS (Fig. 5b) and specifically represent cell membrane phospholipids (722 cm^{-1}), DNA bases (783 cm^{-1}), arginine (991 cm^{-1}) and triglycerides (1300 cm^{-1}) with equivalent representative species from the LC-MS data.³⁵⁻³⁹ We find that for RS and LC-MS, the trends in metabolites for the various sample groups are generally in agreement, which not only shows these two approaches are complimentary but also highlights the strengths and limitations of each method. RS is a low-cost extraction-free approach that allows rapid measurement of cells at the single cell level capturing heterogeneities in treatment response within individual cells with high sensitivity. This allows classification between the various treatment groups with high confidence. However, RS has low specificity in identifying specific metabolites within a similar class. For example, the 1300 cm^{-1} triglyceride peak in RS is a measure of all triglycerides that share a peak in that region,^{35, 37} which may explain the discrepancy between the triglyceride peak intensity distribution for the treated groups and the clear separation observable for LC-MS. However, since LC-MS requires a large quantity of cells with an elaborate extraction approach for accurate measurements, it can be both time- and labor-intensive and cannot resolve heterogeneities in individual cells. Therefore, the synergistic integration of both approaches is highly desirable for holistic understanding of metabolic reprogramming in cancer cells and alterations in metabolites after treatment.

We then examined the metabolic pathways that are enriched via KEGG pathway analysis comparing the untreated and oxaliplatin monotherapy treated datasets from both MS metabolomics, and Raman analysis. For LC-MS, all positively identified human metabolites were used for KEGG analysis (Fig. 6a), and for Raman, the principal peak assignments

corresponding to various metabolites were used (Fig. 6b). Our enrichment analysis show pathways from both datasets are congruent, with 13 out of the 24 top highlighted pathways in Raman that overlap with MS. These include key amino acid metabolism such as phenylalanine metabolism, arginine and histidine metabolism. They also include lipid-associated pathways such as fatty acid biosynthesis, elongation and degradation, and arachidonic acid metabolism. The LC-MS metabolites that are associated with the respective enriched pathways are shown in Table S1, and the Raman metabolites associated with the respective pathways are shown in Table S2. We then compared the enrichment ratios of untreated control vs. the nonresponsive drug CTX, and control vs. combination treatment CTX + OX. Our analysis shows significant differences in enriched pathway analysis (Fig. 6c). Enrichment analysis for control vs. CTX and control vs. combination treatment can be seen in Fig. S7. In these comparative enrichments, the elevated enrichments in the control versus combination treatment indicates that the metabolic pathways are elevated in the untreated cancer cells (and downregulated post treatment). For example, the aminoacyl-tRNA biosynthesis pathway corresponds to inhibition of DNA transcription to RNA due to the cytotoxicity of OX and DNA damage. The enrichment change in purine metabolism also suggests a reduction in DNA synthesis as explained earlier in Fig. 4. Enrichment observed in other pathways is likely also contributed by the apoptotic action of the combinatorial treatment. Arginine biosynthesis, and arginine/proline metabolism were highlighted as modified pathways in both the LC-MS and Raman analysis; abnormal arginine metabolism is a key feature of CRC metabolic reprogramming.⁴⁰ Arginine is a substrate for nitric oxide synthases, which produce nitric oxide which then contributes to proliferative signaling pathways (PI3K-AKT and RAS-RAF-ERK), as well as contributes to apoptosis resistance.⁷¹ p53 activation can inhibit NOS expression; therefore p53-induced activation due to DNA damage could be a contributing factor in these pathway perturbations. Arginine metabolism is also involved in the synthesis of glutamate, nucleotides, polyamines, and proline.⁴⁰ Proline metabolism also influences CRC where proline feeds the cell cycle through conversion to L-pyrroline-5-carboxylate (P5C).⁴⁸ P5C can then be converted to glutamic-gamma-semialdehyde which can be used to produce glutamate and fuel the TCA cycle.⁷² Proline is also involved in anti-tumor metabolism. p53 can induce proline oxidase expression, which uses proline as a substrate to produce reactive oxygen species downregulating proliferative signals and contributing to apoptosis.⁷² Pathways associated with amino acids including histidine, tryptophan, and tyrosine metabolism are also amplified in KRAS-mutant colorectal cancer.⁴² Perturbation and downregulation of these metabolisms may serve as an indicator of a reduction of KRAS-granted anti-EGFR resistance. Similar to amino acid metabolism perturbation, the impact on fatty acid metabolisms is also indicative of treatment response. Fatty acid metabolism is dysregulated in CRC, including an upregulation of *de novo* fatty acid synthesis.⁴⁴ Downregulation of fatty acid synthesis can be a result of down-regulating EGFR-associated MAPK and PI3K proliferative signaling pathways.⁷³ The impact on the nicotinic and nicotinamide is also notable. NAD is produced through both a *de novo* pathway (from tryptophan metabolism) as well as from salvage pathways using nicotinamide and nicotinic acid.⁷⁴ Enzymes that drive these salvage pathways are amplified in colorectal cancer. Due to the short half-life of NAD in cancer cells, biosynthesis of NAD is necessary to maintain tumor growth.⁷⁵ This disruption is consistent with previous work showing a rapid decrease in NAD abundance following

the induction of apoptosis, which suggested an exhaustion of NAD in cell damage repair efforts.⁷⁶

Conclusions

In summary, our study demonstrates the utility of Raman spectroscopy in understanding metabolic changes in human CRC cells that goes beyond the traditional cell viability assays. We map anti-EGFR (cetuximab) resistance in KRAS-mutant CRC cells and develop an approach to reverse the cetuximab resistance by sensitization of cells with chemotherapies. Our Raman measurements combined with multivariate analysis shows that in combination treatment of cetuximab + oxaliplatin, sequential administration of drugs rather than simultaneous delivery is important in achieving effective therapeutic response. Single cell Raman metabolic profiling is validated by ensemble LC-MS metabolomics where both approaches identify key metabolites that are changed in the responsive group but remain unaltered in the resistant group. Metabolic pathways previously found to be impacted by p53 activation were perturbed during oxaliplatin treatment giving support to the hypothesis that DNA-damage facilitated p53 activation contributes to sensitization towards anti-EGFR therapies of KRAS-mutant cancer cells. We also find pathways corresponding to amino acids and fatty acids alter with treatment and may provide mechanisms of anti-EGFR resistance. Further nanomechanical measurements on single cells corroborate trends in metabolic transformation suggesting that cancer cells leverage mechanosensitive metabolism to maintain viability. The results of this work lay the foundation of our future work on tumor spheroids and organotypic cultures that will recapitulate the human tumor microenvironment. Our findings will ultimately apply to CRC patients in identifying metabolic pathways that result in resistance to standard-of-care therapies, and enable treatment combinations that has the potential to overcome drug resistance. Raman spectroscopy can also be implemented in a high throughput manner, and when integrated with sophisticated machine learning algorithms our approach would allow accurate drug screening for *a priori* determination of patients who are likely to be resistant.

Supplementary Material

Refer to Web version on PubMed Central for supplementary material.

Acknowledgements

We acknowledge Eugene C. Lin (Department of Chemistry and Biochemistry, National Chung Cheng University, Chiayi 62106, Taiwan) for assistance in providing data processing files. We acknowledge the W.M. Keck Metabolomics Research Laboratory (Office of Biotechnology, Iowa State University, Ames IA) for providing analytical instrumentation and we thank Dr(s). Ann M Perera, Lucas J Showmnan, and Matthew W Breitzman for their assistance and support. GC acknowledges support from the National Institutes of Health (NIH) award R01EB029756-01A1. NH acknowledges support from the congressionally directed medical research program (CDMRP) award W81XWH-20-1-0620. SU acknowledges support from NIH award R21HD100685-01. BS acknowledges support from the NIH R01 CA248505, American Cancer Society RSG-20-130-01-DDC, and CDMRP W81XWH-21-1-0694. RB acknowledges support from NIH R21HD100685-01, NIH R01EB029756-01A1, and CDMRP W81XWH-20-1-0620 awards.

References

- (1). Dekker E; Tanis PJ; Vleugels JLA; Kasi PM; Wallace MB Colorectal cancer. *The Lancet* 2019, 394 (10207), 1467–1480, DOI: 10.1016/S0140-6736(19)32319-0.
- (2). Ma B; Li Y; Meng Q The predictive and prognostic value of sex in localized colorectal cancer: a SEER-based analysis. *Transl Cancer Res* 2021, 10 (5), 2108–2119, DOI: 10.21037/tcr-20-3421. [PubMed: 35116531]
- (3). Siegel RL; Miller KD; Fuchs HE; Jemal A Cancer statistics, 2022. *CA Cancer J. Clin* 2022, 72 (1), 7–33, DOI: 10.3322/caac.21708. [PubMed: 35020204]
- (4). Kuipers EJ; Grady WM; Lieberman D; Seufferlein T; Sung JJ; Boelens PG; van de Velde CJH; Watanabe T Colorectal cancer. *Nat. Rev. Dis. Primers* 2015, 1 (1), 15065, DOI: 10.1038/nrdp.2015.65. [PubMed: 27189416]
- (5). Xie Y-H; Chen Y-X; Fang J-Y Comprehensive review of targeted therapy for colorectal cancer. *Signal Transduct. Target. Ther* 2020, 5 (1), 22, DOI: 10.1038/s41392-020-0116-z. [PubMed: 32296018]
- (6). Gustavsson B; Carlsson G; Machover D; Petrelli N; Roth A; Schmolli H-J; Tveit K-M; Gibson F A Review of the Evolution of Systemic Chemotherapy in the Management of Colorectal Cancer. *Clin. Colorectal Cancer* 2015, 14 (1), 1–10, DOI: 10.1016/j.clcc.2014.11.002. [PubMed: 25579803]
- (7). Hu T; Li Z; Gao CY; Cho CH Mechanisms of drug resistance in colon cancer and its therapeutic strategies. *World J. Gastroenterol* 2016, 22 (30), 6876–6889, DOI: 10.3748/wjg.v22.i30.6876. [PubMed: 27570424]
- (8). Mohelnikova-Duchonova B; Melichar B; Soucek P FOLFOX/FOLFIRI pharmacogenetics: the call for a personalized approach in colorectal cancer therapy. *World J. Gastroenterol* 2014, 20 (30), 10316–10330, DOI: 10.3748/wjg.v20.i30.10316. [PubMed: 25132748]
- (9). Hon KW; Abu N; Ab Mutalib N-S; Jamal R miRNAs and lncRNAs as Predictive Biomarkers of Response to FOLFOX Therapy in Colorectal Cancer. *Front. Pharmacol* 2018, 9, DOI: 10.3389/fphar.2018.00846. [PubMed: 29422861]
- (10). Martínez-Reyes I; Chandel NS Cancer metabolism: looking forward. *Nat. Rev. Cancer* 2021, 21 (10), 669–680, DOI: 10.1038/s41568-021-00378-6. [PubMed: 34272515]
- (11). DeBerardinis RJ; Chandel NS Fundamentals of cancer metabolism. *Sci. Adv* 2016, 2 (5), e1600200, DOI: 10.1126/sciadv.1600200. [PubMed: 27386546]
- (12). Pavlova NN; Thompson CB The Emerging Hallmarks of Cancer Metabolism. *Cell Metab* 2016, 23 (1), 27–47, DOI: 10.1016/j.cmet.2015.12.006. [PubMed: 26771115]
- (13). Norbert A; Stefanie S; Rebecca R Response to Therapy in Breast Cancer. *J. Nucl. Med* 2009, 50 (Suppl 1), 55S, DOI: 10.2967/jnumed.108.057240. [PubMed: 19380410]
- (14). Cutshaw G; Hassan N; Uthaman S; Kothadiya S; Wen X; Bardhan R The Emerging Role of Raman Spectroscopy as an Omics Approach for Metabolic Profiling and Biomarker Detection towards Precision Medicine. In *Chem. Revs*, 2023.
- (15). Zhang C; Li J; Lan L; Cheng JX Quantification of Lipid Metabolism in Living Cells through the Dynamics of Lipid Droplets Measured by Stimulated Raman Scattering Imaging. *Anal. Chem* 2017, 89 (8), 4502–4507, DOI: 10.1021/acs.analchem.6b04699. [PubMed: 28345862]
- (16). Noothalapati H; Shigeto S Exploring metabolic pathways in vivo by a combined approach of mixed stable isotope-labeled Raman microspectroscopy and multivariate curve resolution analysis. *Anal. Chem* 2014, 86 (15), 7828–7834, DOI: 10.1021/ac501735c. [PubMed: 24975289]
- (17). Pence I; Mahadevan-Jansen A Clinical instrumentation and applications of Raman spectroscopy. *Chem. Soc. Rev* 2016, 45 (7), 1958–1979, DOI: 10.1039/C5CS00581G. [PubMed: 26999370]
- (18). Xu J; Yu T; Zois CE; Cheng J-X; Tang Y; Harris AL; Huang WE Unveiling Cancer Metabolism through Spontaneous and Coherent Raman Spectroscopy and Stable Isotope Probing. *Cancers (Basel)* 2021, 13 (7), DOI: 10.3390/cancers13071718.
- (19). Deng X; Milligan K; Brolo A; Lum JJ; Andrews JL; Jirasek A Radiation treatment response and hypoxia biomarkers revealed by machine learning assisted Raman spectroscopy in tumour cells and xenograft tissues. *Analyst* 2022, 147 (22), 5091–5104, DOI: 10.1039/D2AN01222G. [PubMed: 36217911]

- (20). Larion M; Dowdy T; Ruiz-Rodado V; Meyer MW; Song H; Zhang W; Davis D; Gilbert MR; Lita A Detection of Metabolic Changes Induced via Drug Treatments in Live Cancer Cells and Tissue Using Raman Imaging Microscopy. *Biosensors* 2019, 9 (1), DOI: 10.3390/bios9010005.
- (21). Kanmalar M; Abdul Sani SF; Kamri NINB; Said NABM; Jamil AHBA; Kuppusamy S; Mun KS; Bradley DA Raman spectroscopy biochemical characterisation of bladder cancer cisplatin resistance regulated by FDFT1: a review. *Cell. Mol. Biol. Lett* 2022, 27 (1), 9, DOI: 10.1186/s11658-022-00307-x. [PubMed: 35093030]
- (22). Wei L; Hu F; Shen Y; Chen Z; Yu Y; Lin C-C; Wang MC; Min W Live-cell imaging of alkyne-tagged small biomolecules by stimulated Raman scattering. *Nat. Methods* 2014, 11 (4), 410–412, DOI: 10.1038/nmeth.2878. [PubMed: 24584195]
- (23). Ami D; Duse A; Mereghetti P; Cozza F; Ambrosio F; Ponzini E; Grandori R; Lunetta C; Tavazzi S; Pezzoli F; et al. Tear-Based Vibrational Spectroscopy Applied to Amyotrophic Lateral Sclerosis. *Anal. Chem* 2021, 93 (51), 16995–17002, DOI: 10.1021/acs.analchem.1c02546. [PubMed: 34905686]
- (24). Ali A; Abouleila Y; Shimizu Y; Hiyama E; Watanabe TM; Yanagida T; Germond A Single-Cell Screening of Tamoxifen Abundance and Effect Using Mass Spectrometry and Raman Spectroscopy. *Anal. Chem* 2019, 91 (4), 2710–2718, DOI: 10.1021/acs.analchem.8b04393. [PubMed: 30664349]
- (25). Ou Y-C; Wen X; Johnson CA; Shae D; Ayala OD; Webb JA; Lin EC; DeLapp RC; Boyd KL; Richmond A; et al. Multimodal Multiplexed Immunoinaging with Nanostars to Detect Multiple Immunomarkers and Monitor Response to Immunotherapies. *ACS Nano* 2020, 14 (1), 651–663, DOI: 10.1021/acsnano.9b07326. [PubMed: 31851488]
- (26). Wen X; Ou Y-C; Zarick HF; Zhang X; Hmelo AB; Victor QJ; Paul EP; Slocik JM; Naik RR; Bellan LM; et al. PRADA: Portable Reusable Accurate Diagnostics with nanostar Antennas for multiplexed biomarker screening. *Bioeng. Transl. Med* 2020, 5 (3), e10165, DOI: 10.1002/btm2.10165. [PubMed: 33005736]
- (27). Ou Y-C; Webb JA; O'Brien CM; Pence IJ; Lin EC; Paul EP; Cole D; Ou S-H; Lapierre-Landry M; DeLapp RC; et al. Diagnosis of immunomarkers in vivo via multiplexed surface enhanced Raman spectroscopy with gold nanostars. *Nanoscale* 2018, 10 (27), 13092–13105, DOI: 10.1039/C8NR01478G. [PubMed: 29961778]
- (28). Hammoud MK; Yosef HK; Lechtonen T; Aljakouch K; Schuler M; Alsaidi W; Daho I; Maghnouj A; Hahn S; El-Mashtoly SF; et al. Raman micro-spectroscopy monitors acquired resistance to targeted cancer therapy at the cellular level. *Sci. Rep* 2018, 8 (1), 15278, DOI: 10.1038/s41598-018-33682-7. [PubMed: 30323297]
- (29). El-Mashtoly SF; Yosef HK; Petersen D; Mavarani L; Maghnouj A; Hahn S; Kötting C; Gerwert K Label-Free Raman Spectroscopic Imaging Monitors the Integral Physiologically Relevant Drug Responses in Cancer Cells. *Anal. Chem* 2015, 87 (14), 7297–7304, DOI: 10.1021/acs.analchem.5b01431. [PubMed: 26075314]
- (30). Mondol AS; El-Mashtoly SF; Frick T; Gerwert K; Popp J; Schie IW High-content screening Raman spectroscopy (HCS-RS) of panitumumab-exposed colorectal cancer cells. *Analyst* 2019, 144 (20), 6098–6107, DOI: 10.1039/C9AN01176E. [PubMed: 31531499]
- (31). Aljakouch K; Lechtonen T; Yosef HK; Hammoud MK; Alsaidi W; Kötting C; Mügge C; Kourist R; El-Mashtoly SF; Gerwert K Raman Microspectroscopic Evidence for the Metabolism of a Tyrosine Kinase Inhibitor, Neratinib, in Cancer Cells. *Angew. Chem. Int. Ed* 2018, 57 (24), 7250–7254, DOI: 10.1002/anie.201803394.
- (32). Zanutelli MR; Zhang J; Reinhart-King CA Mechanoresponsive metabolism in cancer cell migration and metastasis. *Cell Metab* 2021, 33 (7), 1307–1321, DOI: 10.1016/j.cmet.2021.04.002. [PubMed: 33915111]
- (33). Zhang L; Henson MJ; Sekulic SS Multivariate data analysis for Raman imaging of a model pharmaceutical tablet. *Anal. Chim. Acta* 2005, 545 (2), 262–278, DOI: 10.1016/j.aca.2005.04.080.
- (34). Kumar S; Verma T; Mukherjee R; Ariese F; Somasundaram K; Umopathy S Raman and infra-red microspectroscopy: towards quantitative evaluation for clinical research by ratiometric analysis. *Chem. Soc. Rev* 2016, 45 (7), 1879–1900, DOI: 10.1039/C5CS00540J. [PubMed: 26497386]

- (35). Movasaghi Z; Rehman S; Rehman IU Raman Spectroscopy of Biological Tissues. *Appl. Spectrosc. Rev* 2007, 42 (5), 493–541, DOI: 10.1080/05704920701551530.
- (36). De Gelder J; De Gussem K; Vandenabeele P; Moens L Reference database of Raman spectra of biological molecules. *J. Raman Spectrosc* 2007, 38 (9), 1133–1147, DOI: 10.1002/jrs.1734.
- (37). Czamara K; Majzner K; Pacia MZ; Kochan K; Kaczor A; Baranska M Raman spectroscopy of lipids: a review. *J. Raman Spectrosc* 2015, 46 (1), 4–20, DOI: 10.1002/jrs.4607.
- (38). Ricciardi A; Piuri G; Porta MD; Mazzucchelli S; Bonizzi A; Truffi M; Sevieri M; Allevi R; Corsi F; Cazzola R; et al. Raman spectroscopy characterization of the major classes of plasma lipoproteins. *Vib. Spectrosc* 2020, 109, 103073, DOI: 10.1016/j.vibspec.2020.103073.
- (39). Zhu G; Zhu X; Fan Q; Wan X Raman spectra of amino acids and their aqueous solutions. *Spectrochimica Acta Part A: Molecular and Biomolecular Spectroscopy* 2011, 78 (3), 1187–1195, DOI: 10.1016/j.saa.2010.12.079. [PubMed: 21242101]
- (40). Du T; Han J Arginine Metabolism and Its Potential in Treatment of Colorectal Cancer. *Front Cell Dev Biol* 2021, 9, 658861, DOI: 10.3389/fcell.2021.658861. [PubMed: 34095122]
- (41). Currie E; Schulze A; Zechner R; Walther Tobias C.; Farese Robert V. Jr. Cellular Fatty Acid Metabolism and Cancer. *Cell Metab* 2013, 18 (2), 153–161, DOI: 10.1016/j.cmet.2013.05.017. [PubMed: 23791484]
- (42). Kundu S; Ali MA; Handin N; Conway LP; Rendo V; Artursson P; He L; Globisch D; Sjöblom T Common and mutation specific phenotypes of KRAS and BRAF mutations in colorectal cancer cells revealed by integrative -omics analysis. *J. Exp. Clin. Cancer Res* 2021, 40 (1), 225, DOI: 10.1186/s13046-021-02025-2. [PubMed: 34233735]
- (43). Lutz NW; Tome ME; Cozzone PJ Early changes in glucose and phospholipid metabolism following apoptosis induction by IFN- γ /TNF- α in HT-29 cells. *FEBS Lett* 2003, 544 (1), 123–128, DOI: 10.1016/S0014-5793(03)00489-7. [PubMed: 12782301]
- (44). Krauß D; Fari O; Sibilina M Lipid Metabolism Interplay in CRC - An Update. *Metabolites* 2022, 12 (3), DOI: 10.3390/metabo12030213.
- (45). Chen D; Zhou X; Yan P; Yang C; Li Y; Han L; Ren X Lipid metabolism reprogramming in colorectal cancer. *J. Cell. Biochem* 2023, 124 (1), 3–16, DOI: 10.1002/jcb.30347. [PubMed: 36334309]
- (46). Huang C; Freter C Lipid metabolism, apoptosis and cancer therapy. *Int. J. Mol. Sci* 2015, 16 (1), 924–949, DOI: 10.3390/ijms16010924. [PubMed: 25561239]
- (47). Zhang J; Zou S; Fang L Metabolic reprogramming in colorectal cancer: regulatory networks and therapy. *Cell Biosci* 2023, 13 (1), 25, DOI: 10.1186/s13578-023-00977-w. [PubMed: 36755301]
- (48). D'Aniello C; Patriarca EJ; Phang JM; Minchiotti G Proline Metabolism in Tumor Growth and Metastatic Progression. *Front. Oncol* 2020, 10, DOI: 10.3389/fonc.2020.00776.
- (49). Liu C; Jin Y; Fan Z The Mechanism of Warburg Effect-Induced Chemoresistance in Cancer. *Front. Oncol* 2021, 11, DOI: 10.3389/fonc.2021.698023.
- (50). Schoch S; Gajewski S; Rothfuß J; Hartwig A; Köberle B Comparative Study of the Mode of Action of Clinically Approved Platinum-Based Chemotherapeutics. *Int. J. Mol. Sci* 2020, 21 (18), DOI: 10.3390/ijms21186928.
- (51). Hsu H-H; Chen M-C; Baskaran R; Lin Y-M; Day CH; Lin Y-J; Tu C-C; Vijaya Padma V; Kuo W-W; Huang C-Y Oxaliplatin resistance in colorectal cancer cells is mediated via activation of ABCG2 to alleviate ER stress induced apoptosis. *J. Cell. Physiol* 2018, 233 (7), 5458–5467, DOI: 10.1002/jcp.26406. [PubMed: 29247488]
- (52). Kelland L The resurgence of platinum-based cancer chemotherapy. *Nat. Rev. Cancer* 2007, 7 (8), 573–584, DOI: 10.1038/nrc2167. [PubMed: 17625587]
- (53). Deng X; Kong F; Li S; Jiang H; Dong L; Xu X; Zhang X; Yuan H; Xu Y; Chu Y; et al. A KLF4/PiHL/EZH2/HMGA2 regulatory axis and its function in promoting oxaliplatin-resistance of colorectal cancer. *Cell Death Dis* 2021, 12 (5), 485, DOI: 10.1038/s41419-021-03753-1. [PubMed: 33986248]
- (54). Yin C; Lu W; Ma M; Yang Q; He W; Hu Y; Xia L Efficacy and mechanism of combination of oxaliplatin with PKM2 knockdown in colorectal cancer. *Oncol. Lett* 2020, 20 (6), 312, DOI: 10.3892/ol.2020.12175. [PubMed: 33093921]

- (55). Al-Saffar NM; Titley JC; Robertson D; Clarke PA; Jackson LE; Leach MO; Ronen SM Apoptosis is associated with triacylglycerol accumulation in Jurkat T-cells. *Br. J. Cancer* 2002, 86 (6), 963–970, DOI: 10.1038/sj.bjc.6600188. [PubMed: 11953830]
- (56). Duarte IF; Lamego I; Marques J; Marques MP; Blaise BJ; Gil AM Nuclear magnetic resonance (NMR) study of the effect of cisplatin on the metabolic profile of MG-63 osteosarcoma cells. *J. Proteome Res* 2010, 9 (11), 5877–5886, DOI: 10.1021/pr100635n. [PubMed: 20815413]
- (57). Zhu G; Pei L; Xia H; Tang Q; Bi F Role of oncogenic KRAS in the prognosis, diagnosis and treatment of colorectal cancer. *Mol. Cancer* 2021, 20 (1), 143, DOI: 10.1186/s12943-021-01441-4. [PubMed: 34742312]
- (58). Narvi E; Vaparanta K; Karrila A; Chakroborty D; Knuutila S; Pulliainen A; Sundvall M; Elenius K Different responses of colorectal cancer cells to alternative sequences of cetuximab and oxaliplatin. *Sci. Rep* 2018, 8 (1), 16579, DOI: 10.1038/s41598-018-34938-y. [PubMed: 30410004]
- (59). Dienstmann R; Salazar R; Tabernero J Overcoming Resistance to Anti-EGFR Therapy in Colorectal Cancer. In *American Society of Clinical Oncology Educational Book*, Wolters Kluwer, 2015; pp e149–e156.
- (60). Ward PS; Thompson CB Metabolic reprogramming: a cancer hallmark even warburg did not anticipate. *Cancer Cell* 2012, 21 (3), 297–308, DOI: 10.1016/j.ccr.2012.02.014. [PubMed: 22439925]
- (61). Bertero T; Gaggioli C Mechanical forces rewire metabolism in the tumor niche. *Mol. Cell. Oncol* 2019, 6 (3), 1592945, DOI: 10.1080/23723556.2019.1592945. [PubMed: 31131310]
- (62). Ge H; Tian M; Pei Q; Tan F; Pei H Extracellular Matrix Stiffness: New Areas Affecting Cell Metabolism. *Front. Oncol* 2021, 11, 631991, DOI: 10.3389/fonc.2021.631991. [PubMed: 33718214]
- (63). Nahar S; Schmetz A; Schitter G; Skarpas A Quantitative nanomechanical property mapping of bitumen micro-phases by peak-force Atomic Force Microscopy. In *International Conference on Asphalt Pavements*, 2014.
- (64). Young TJ; Monclus MA; Burnett TL; Broughton WR; Ogin SL; Smith PA The use of the PeakForce™ quantitative nanomechanical mapping AFM-based method for high-resolution Young's modulus measurement of polymers. *Meas. Sci. Technol* 2011, 22 (12), 125703, DOI: 10.1088/0957-0233/22/12/125703.
- (65). Hu J; Chen S; Huang D; Zhang Y; Lü S; Long M Global mapping of live cell mechanical features using PeakForce QNM AFM. *Biophysics Reports* 2020, 6 (1), 9–18, DOI: 10.1007/s41048-019-00103-9.
- (66). Kontomaris SV The Hertz Model in AFM Nanoindentation Experiments: Applications in Biological Samples and Biomaterials. *Micro and Nanosystems* 2018,
- (67). Gavara N; Chadwick RS Determination of the elastic moduli of thin samples and adherent cells using conical atomic force microscope tips. *Nat Nanotechnol* 2012, 7 (11), 733–736, DOI: 10.1038/nnano.2012.163. [PubMed: 23023646]
- (68). Ayee MA; Levitan I Paradoxical impact of cholesterol on lipid packing and cell stiffness. *FBL* 2016, 21 (6), 1245–1259, DOI: 10.2741/4454. [PubMed: 27100504]
- (69). Kim HR; Roe JS; Lee JE; Hwang IY; Cho EJ; Youn HD A p53-inducible microRNA-34a downregulates Ras signaling by targeting IMPDH. *Biochem Biophys Res Commun* 2012, 418 (4), 682–688, DOI: 10.1016/j.bbrc.2012.01.077. [PubMed: 22301190]
- (70). Cotte AK; Aires V; Fredon M; Limagne E; Derangère V; Thibaudin M; Humblin E; Scagliarini A; de Barros J-PP; Hillon P; et al. Lysophosphatidylcholine acyltransferase 2-mediated lipid droplet production supports colorectal cancer chemoresistance. *Nat. Commun* 2018, 9 (1), 322, DOI: 10.1038/s41467-017-02732-5. [PubMed: 29358673]
- (71). Fukumura D; Kashiwagi S; Jain RK The role of nitric oxide in tumour progression. *Nat. Rev. Cancer* 2006, 6 (7), 521–534, DOI: 10.1038/nrc1910. [PubMed: 16794635]
- (72). Phang JM; Liu W Proline metabolism and cancer. *Front Biosci (Landmark Ed)* 2012, 17 (5), 1835–1845, DOI: 10.2741/4022. [PubMed: 22201839]

- (73). Paulina M; Katarzyna D; Alicja P; Adriana M; Tomasz Inhibitors of Fatty Acid Synthesis and Oxidation as Potential Anticancer Agents in Colorectal Cancer Treatment. *Anticancer Res* 2020, 40 (9), 4843, DOI: 10.21873/anticancerres.14487. [PubMed: 32878772]
- (74). Li X.-q.; Lei J; Mao L.-h.; Wang Q.-l.; Xu F; Ran T; Zhou Z.-h.; He S NAMPT and NAPRT, Key Enzymes in NAD Salvage Synthesis Pathway, Are of Negative Prognostic Value in Colorectal Cancer. *Front. Oncol* 2019, 9, DOI: 10.3389/fonc.2019.00736.
- (75). Wei Y; Xiang H; Zhang W Review of various NAMPT inhibitors for the treatment of cancer. *Front. Pharmacol* 2022, 13, DOI: 10.3389/fphar.2022.970553.
- (76). Ronen SM; DiStefano F; McCoy CL; Robertson D; Smith TAD; Al-Saffar NM; Titley J; Cunningham DC; Griffiths JR; Leach MO; et al. Magnetic resonance detects metabolic changes associated with chemotherapy-induced apoptosis. *Br. J. Cancer* 1999, 80 (7), 1035–1041, DOI: 10.1038/sj.bjc.6690459. [PubMed: 10362112]

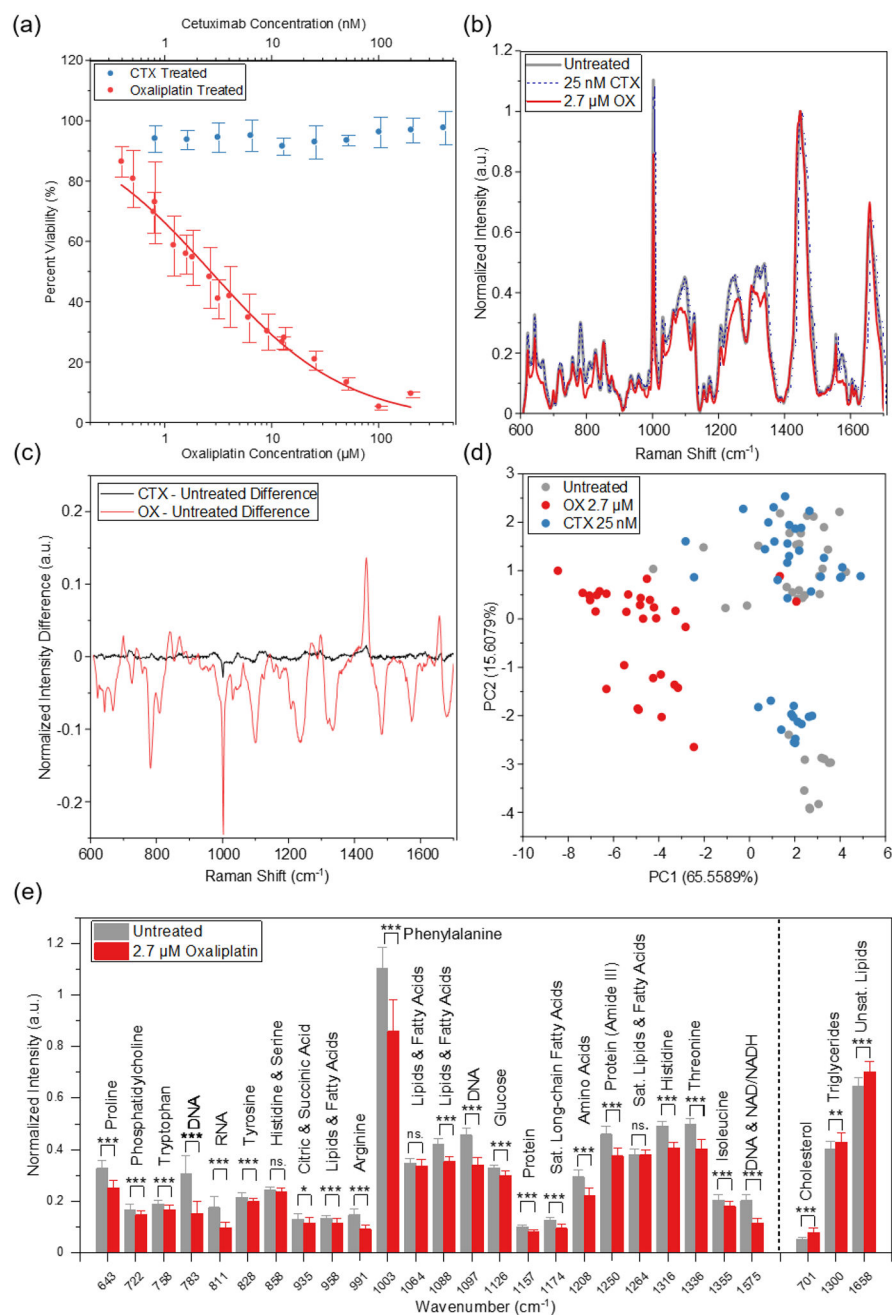
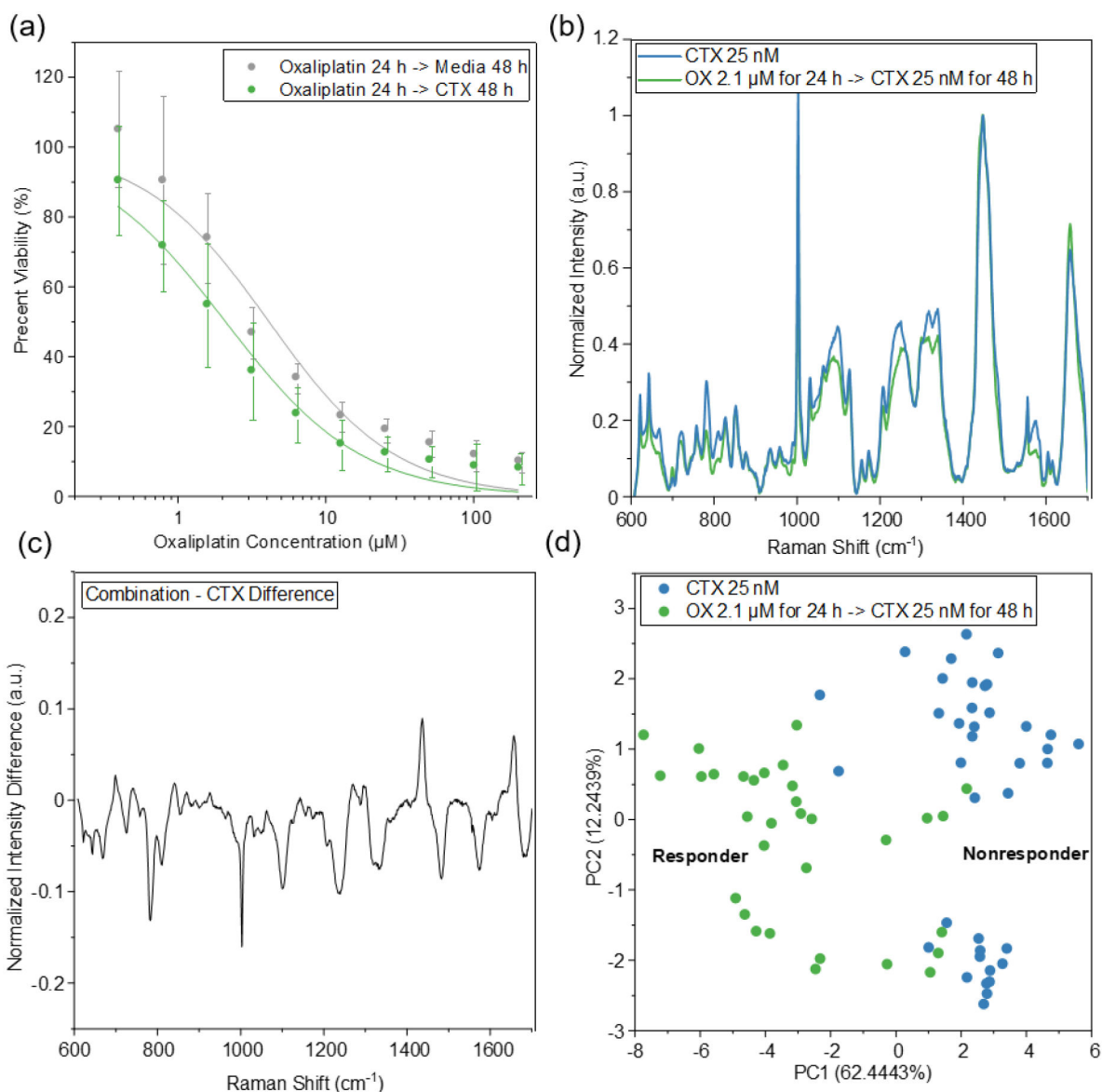


Figure 1: Oxaliplatin (OX) or Cetuximab (CTX) monotherapy. (a) Dose-dependent CCK-8 cell viability assay in HCT116 cells after treatment with cetuximab (CTX) for 48 h (blue curve), and with Oxaliplatin (OX) for 48 h (red curve). The IC₅₀ with OX treatment was 2.69 μM, and cells were resistant to CTX. (b) Average Raman spectra of HCT116 cells after treatment with Oxaliplatin for 48 h at IC₅₀ (red) (n = 31 cells); treatment with 25 nM of Cetuximab for 48 h (dotted blue) (n = 38 cells); and untreated control (grey) (n = 36 cells) (c) Difference spectra obtained by subtracting the averaged control spectra from OX treated spectra (red), and difference spectra between the averaged control spectra and CTX-treated

spectra (black). (d) PCA of untreated control, and cells treated with OX and with CTX. Each dot represents the averaged spectrum of one cell. (e) Key Raman peaks that either increase or decrease in OX treated samples relative to untreated control A student's t-test with a FDR correction was used for statistical analysis; here *ns* refers to not significant. ns.: p > 0.05, *: p < 0.05, **: p < 0.01, ***: p < 0.001.

**Figure 2:**

OX + CTX combination therapy. (a) Dose-dependent CCK-8 cell viability assay vs. Oxaliplatin concentration of HCT116 cells after treatment with Oxaliplatin for 24 h and then with CTX at 25 nM for 48 h. (b) Average Raman spectra of HCT116 cells (green line) after treatment with Oxaliplatin at 2.1 μM for 24 h then with CTX at 25 nM for 48 h ($n = 32$ cells), compared to average Raman spectra of HCT116 with CTX treatment (blue line) ($n = 38$ cells). (c) Difference spectra obtained by subtracting the CTX control spectra from OX+ CTX combination treated spectra. (d) PCA of the two groups; plot of PCA component 1 and 2: CTX treated cells (blue; nonresponder) and combination-treated cells (green; responders).

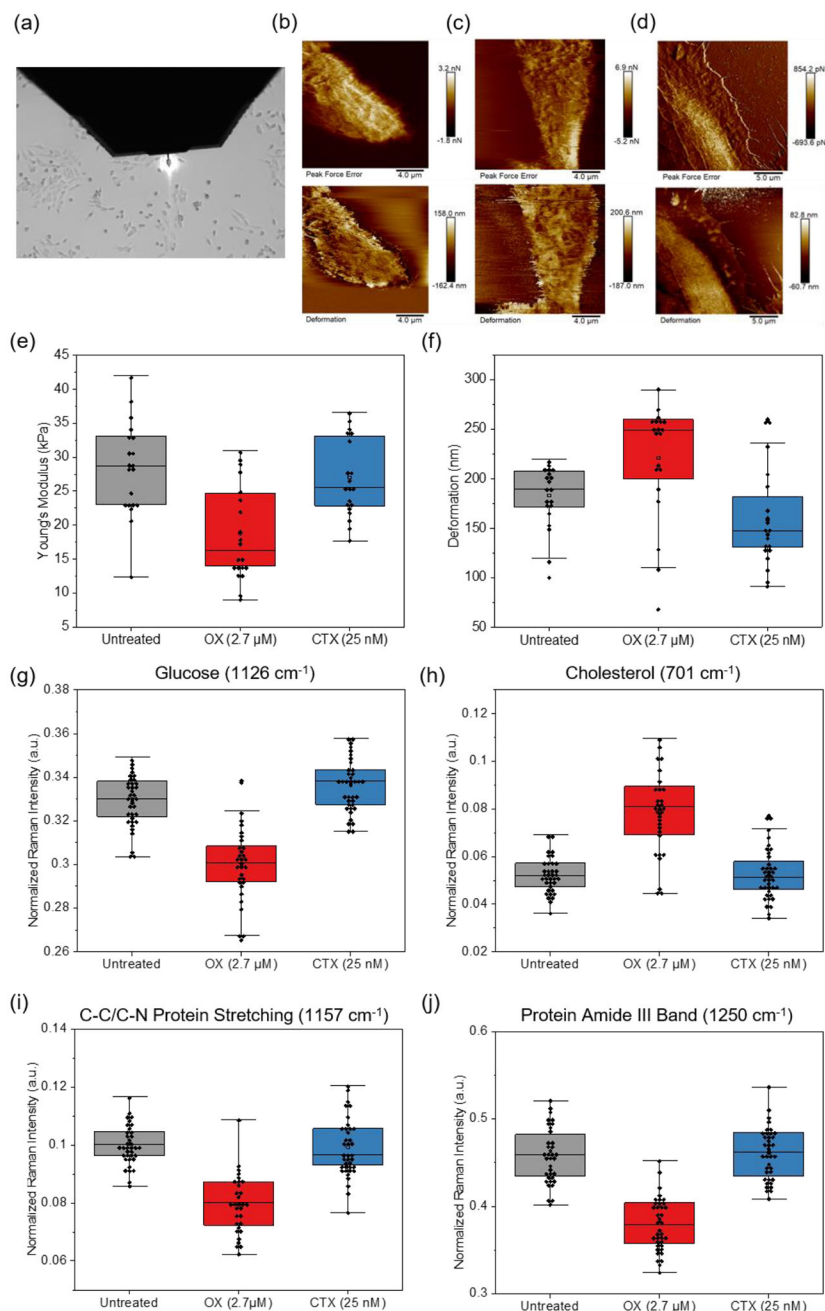


Figure 3. Characterization of nanomechanical properties of HCT116 cells treated with responsive drug, OX, and nonresponsive drug, CTX, relative to untreated control. (a) Brightfield microscope image showing AFM cantilever tip (PFQNM-LC-A-CAL) approaching the live cell surface. (b-d) Shows the peak force error and deformation images of HCT116 cells (b) untreated control ($n = 20$ cells), (c) treated with OX ($n = 20$ cells), and (d) treated with CTX ($n = 20$ cells) respectively. (e) Young's modulus, and (f) deformation of HCT116 cells untreated control, treated with OX (responsive drug), and treated with CTX (nonresponsive drug). (g-j) Select Raman peaks representing key metabolites that alter with changes in

cancer cell mechanics including (g) glucose (1126 cm^{-1}), (h) cholesterol (701 cm^{-1}), (i) C-C/C-N stretching in proteins (1157 cm^{-1}) and (j) Amide III mode in proteins (1250 cm^{-1}).

Author Manuscript

Author Manuscript

Author Manuscript

Author Manuscript

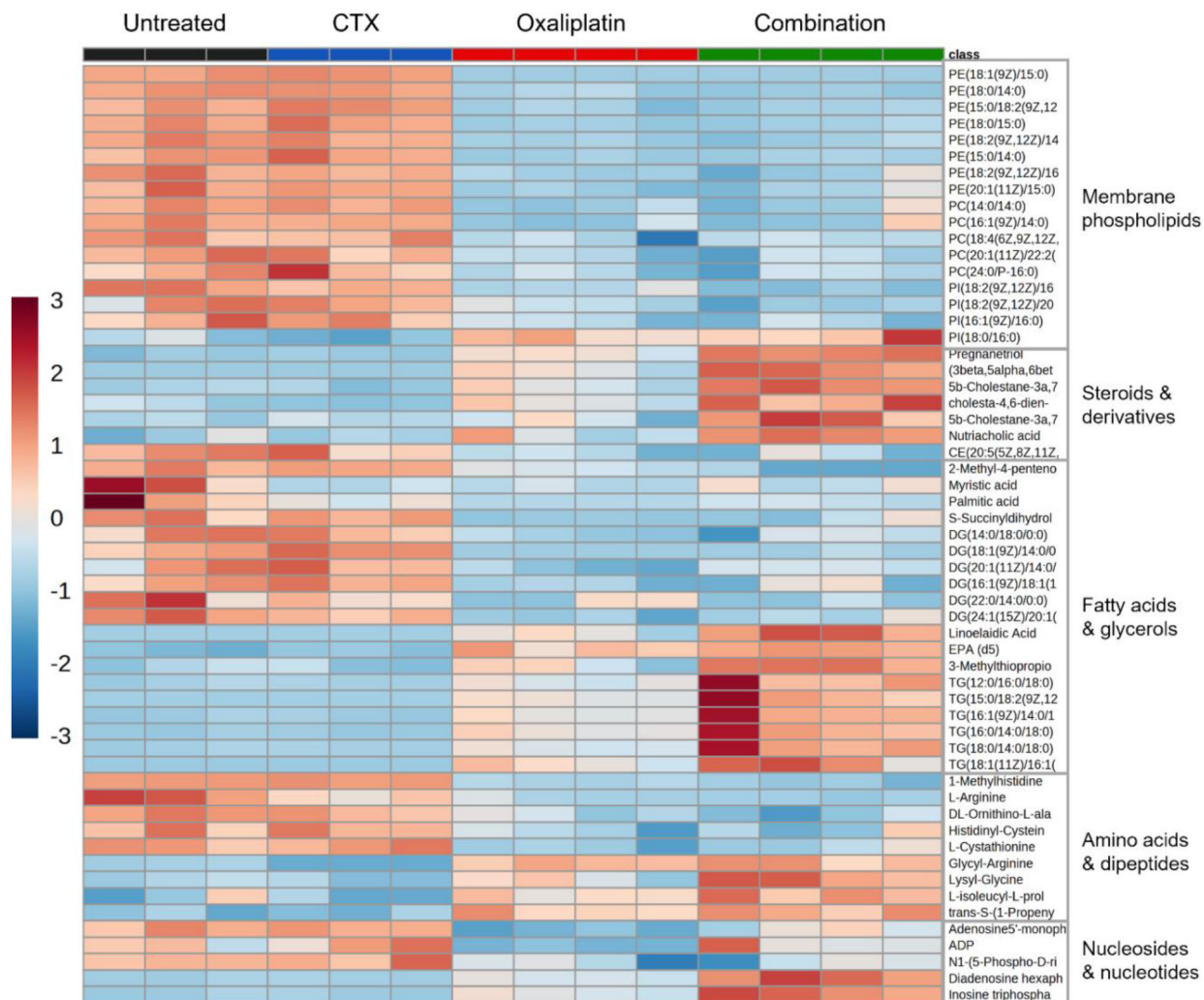


Figure 4. Heat map of LC-MS metabolomics data showing various classes of metabolites from various groups that include control untreated cells (n = 3 samples), cells treated with 25 nM CTX (n = 3 samples), cells treated with 2.7 μ M OX (n = 4 samples) and cells treated with CTX + OX combination (n = 4 samples). Abbreviations: PC (phosphatidylcholine), PE (phosphatidylethanolamine), PI (phosphatidylinositol), DG (diacylglycerol), and TG (triacylglycerol).

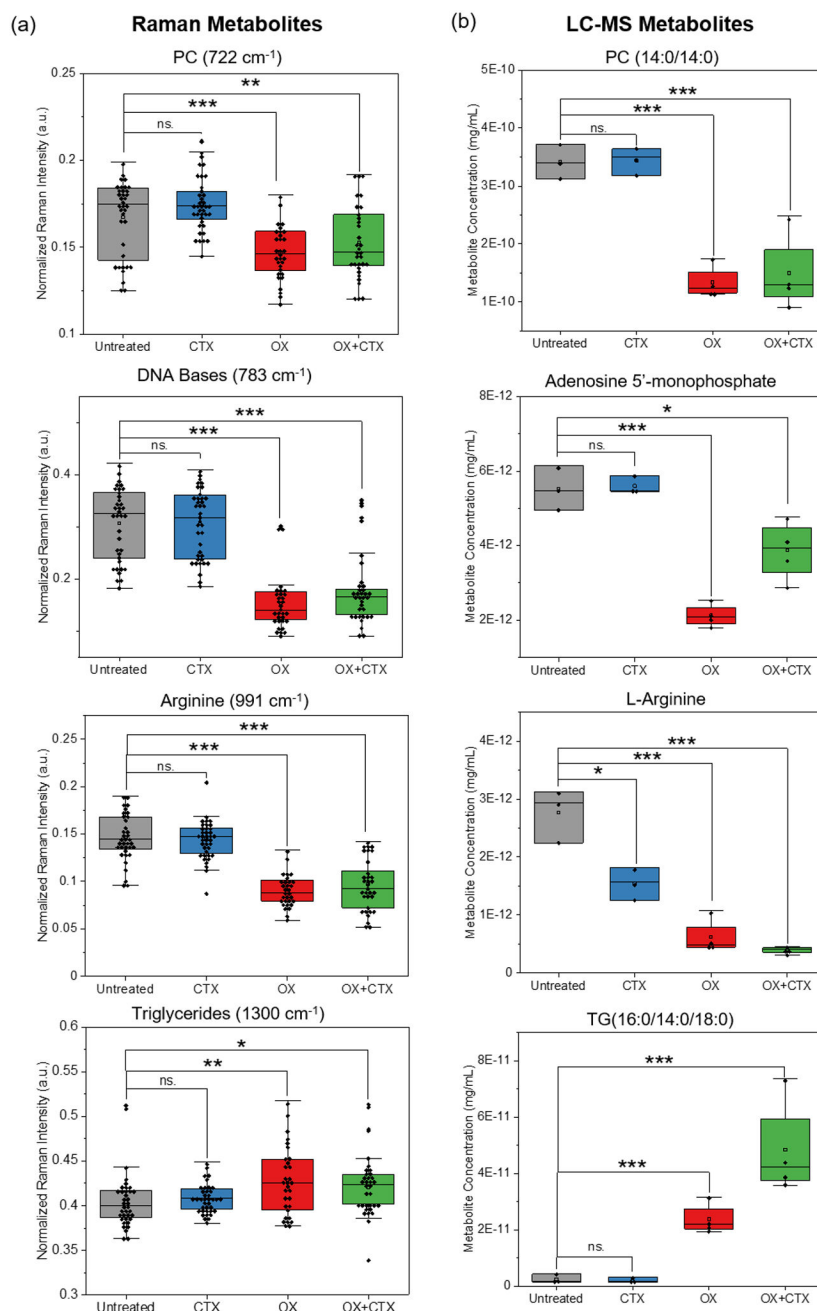
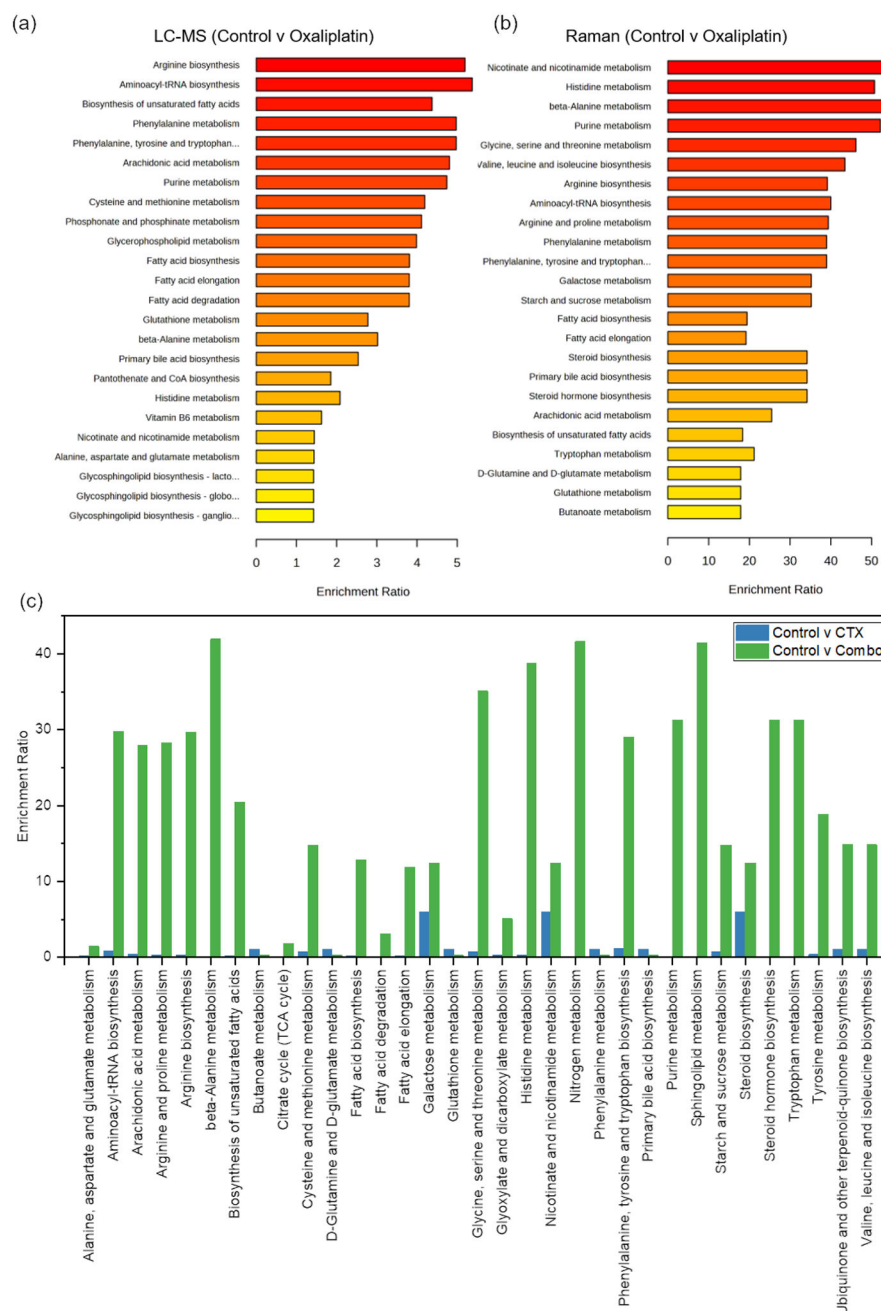


Figure 5.

(a) The ratiometric analysis of Raman spectra compared to that of LC-MS metabolomics. Raman data includes four groups; group 1: untreated control, group 2: CTX (25 nM), group 3: OX (2.7 μ M), group 4: CTX + OX combination. (b) The ratiometric analysis of LC-MS data includes control untreated cells (n = 3 samples), cells treated with 25 nM CTX (n = 3 samples), cells treated with 2.7 μ M OX (n = 4 samples) and cells treated with CTX + OX combination (n = 4 samples). A student's t-test with a FDR correction was used for statistical analysis; here *ns* refers to not significant. *ns*: p > 0.05, *: p < 0.05, **: p < 0.01, ***: p < 0.001.

**Figure 6.**

(a) KEGG pathway enrichment analysis based on LC-MS metabolite measurements of untreated control cells (n = 3 samples) and cells treated with OX (n = 4 samples). (b) KEGG pathway enrichment analysis based on Raman peaks corresponding to metabolites for untreated control cells (n = 33 cells) and cells treated with OX (n = 31 cells). (c) KEGG pathway enrichment analysis based on Raman metabolites comparing two groups: group 1 - untreated control cells (n=30 cells) vs. cells treated with CTX (n = 38 cells), and group 2 - untreated control cells (n = 33 cells) vs. cells treated with CTX + OX combination (n = 32

cells). Here increased enrichments in group 2 indicates that the pathways are elevated in the untreated cancer cells compared to after combination treatment.

Author Manuscript

Author Manuscript

Author Manuscript

Author Manuscript

Table 1.

Peak assignments and corresponding vibrational modes of Raman spectral data.

Wavenumber (cm ⁻¹)	Metabolite	Molecular Structure	Reference
622	Phenylalanine	C-C twisting mode	35,36,39
643	Proline	C-C twisting mode	35,36,39
668	DNA	C-S stretching mode	35,36
701	Cholesterol	Cholesterol ring	35–37
722	Phosphatidylcholine	C-C-N+ symmetric stretching	35–37
758	Tryptophan	Symmetric breathing	35,36
783	DNA	Ring breathing modes	35
811	RNA	O-P-O stretching	35
828	Tyrosine	Ring breathing	35,39
854	Histidine/serine	C-C stretching	35,39
875	Glutamic acid	N ⁺ (CH ₃) ₃ stretching	35,37,39
937	Citric/Succinic Acid	C-H bending	36
958	Lipids and Fatty Acids	CH ₂ bending	37
991	Arginine	C-N stretching	36,39
1003	Phenylalanine	C-C stretching, ring breathing	35,36,39
1031	Phenylalanine	C-H in-plane bending	35,36,39
1064	Lipids and Fatty Acids	C-C skeletal stretch	35,37
1087	Lipids	C-C stretching	35,37
1097	DNA	PO ₂ ⁻ stretch	35
1126	Glucose	C-N stretching	35,36
1157	Protein	C-C/C-N stretch	35,36
1174	Saturated lipids	C-C stretch	35–37
1208	Amino Acids	NH ₃ asymmetric rocking	35
1250	Protein (Amide III)	C-N stretching; N-H bending	35
1264	Fatty acids	C-C stretching, C-H stretching, =CH deformation	37,38
1300	Triglycerides	CH ₂ twisting and bending	35,37
1316	Histidine	CH ₃ /CH ₂ twisting and wagging	36,39
1340	Threonine	CH ₃ /CH ₂ twisting and wagging	36,39
1355	Isoleucine	CH ₃ /CH ₂ twisting and wagging	36,38,39
1448	Lipids & Proteins	CH ₂ and CH ₂ CH ₃ bending, scissoring and deformation.	35,37,38
1555	Tryptophan	C=C vibration	35,36,39
1575	DNA & NADH	Ring breathing modes	35,36
1605	Phenylalanine	Ring C-C stretch	35,36,39
1616	Tyrosine	C=C stretch	35,36,39
1658	Unsaturated Fatty acids	C=O, C=C stretch	35–38